Available online at www.sciencedirect.com
SCIENCE DIRECT
Earth and Planetary Science Letters 244 (2006) 709–724
EPSL
www.elsevier.com/locate/epsl

Electrical tomography of La Soufrière of Guadeloupe Volcano: Field experiments, 1D inversion and qualitative interpretation

Florence Nicollin [a,*], Dominique Gibert [a], François Beauducel [b,c], Georges Boudon [c], Jean-Christophe Komorowski [c]

[a] *Géosciences Rennes (CNRS UMR 6118), Université Rennes 1, Bât. 15 Campus de Beaulieu, 35042 Rennes Cedex, France*
[b] *Observatoire Volcanologique et Sismologique de Guadeloupe (IPGP), Le Houëlmont, 97113 Gourbeyre, Guadeloupe, France*
[c] *Institut de Physique du Globe de Paris (IPGP), CNRS, Equipe Volcanologie, Boîte 89, 4 place Jussieu, 75252 Paris Cedex 05, France*

Received 23 May 2005; received in revised form 6 February 2006; accepted 14 February 2006
Available online 29 March 2006
Editor: V. Courtillot

Abstract

The Soufrière of Guadeloupe lava dome consists of several 3D domains of relatively unaltered massive andesite separated by major radial fractures that reach at least up to about half of the dome's height. More than 20,000 geo-electrical measurements made on the top and the flanks of the lava dome are used to construct the first geophysical image of the internal structure of this active volcano. The main features of the apparent conductivity structure of the lava dome are high-conductivity regions associated with the strongly altered material of present and fossil hydrothermal zones. Local 1D inversions of data subsets belonging to regions where the geological structure is supposed laterally invariant confirm the structures observed in the pseudo-sections. The relatively stable units lie above a basal inclined layer of highly conductive geological materials interpreted to be more altered and thus characterised by reduced internal friction and probably increased pore pressure. Past and current hydrothermal fluid circulation through these fractures has promoted rock alteration and particularly along the base of the dome that likely contributes to the instability of parts of the edifice.

PACS: 02.70.Uu; 02.30.Zz; 91.25.Qi; 91.35.Pn; 91.40.-k; 93.30.Vs
Keywords: electrical tomography; volcano; Guadeloupe; hydrothermal system; inverse problem; simulated annealing

1. Introduction

La Grande Découverte – La Soufrière composite volcano located on the Basse – Terre Island of Guadeloupe is one of the active volcanoes of the recent inner arc in the Lesser Antilles. The IPGP (Observatoire Volcanologique et Sismologique de Guadeloupe) maintains an extensive integrated monitoring network on this volcano located within 5 to 9 km North of the towns of Saint-Claude and Basse-Terre (population of 25,000). The Soufrière lava dome (1467 m, highest point of the Lesser Antilles) was formed during the last magmatic eruption of this volcano dated around 1440 AD [1–3]. The lava dome is cut by several radial fractures that opened during the successive six historical phreatic explosive eruptions of 1690, 1797–98, 1812, 1836–37, 1956, 1976–77 AD.

* Corresponding author. Tel.: +33 2 23 236784; fax: +33 2 23 236090.
E-mail addresses: florence.nicollin@univ-rennes1.fr (F. Nicollin), dominique.gibert@univ-rennes1.fr (D. Gibert), beauducel@ipgp.jussieu.fr (F. Beauducel), boudon@ipgp.jussieu.fr (G. Boudon), komorow@ipgp.jussieu.fr (J.-C. Komorowski).

0012-821X/$ - see front matter © 2006 Elsevier B.V. All rights reserved.
doi:10.1016/j.epsl.2006.02.020

The most substantial eruptions occurred in 1797–98, 1956, and 1976–77. Different fractures or portions of fractures have been newly opened or reactivated during these eruptions, sometimes repeatedly (Fig. 1). Only the central phreatic crater (the Tarissan crater) was active in all eruptions. During the last 1976–1977 crisis, the so-called July 8th and August 30th fractures opened in the eastern and south-eastern part of the lava dome, partly reactivating a fracture formed to east during the 1956 eruption.

The intense hydrothermal activity associated with acidic fumaroles and hot springs that has developed in the last 10,000 yrs at the periphery and base of the lava dome, below the lava dome, and within the fractures on the lava dome has led to extensive argilization of geological formations enhanced by the about 10 m of rainfall per year. Historical observations show that the nature, distribution, and intensity of these geothermal manifestations has fluctuated considerably over time [2,4–6].

Phases of fumarolic reactivation were reported in 1737–1766, 1809–1812, 1879, 1890, 1896, 1899 and 1902–1903. Between the end of the 1976–77 eruption and 1984 there was a phase of progressive decline in fumarolic activity in all areas on the summit (Tarissan, Cratère Sud, Fente du Nord, Cratère 1956), on the flanks (disappearance of the Lacroix fumaroles in 1984) and at the base of the lava dome (disappearance of the Carbet fumaroles in 1979, of the Collardeau fumaroles in 1982, and of the Col de l'échelle fumaroles in 1984). A phase of minimum fumarolic activity occurred between 1984 and 1992, with no fumaroles at the summit and only minor degassing along the SW regional La Ty fracture that intersects the base of the lava dome (fumaroles of the Route de la Citerne and of the Morne Mitan) [5,7].

A phase of systematic progressive increase in fumarolic degassing with reactivation of summit fumaroles began in 1992 at Cratère Sud [5,7], continued in 1996–97 at Napoléon Fracture/Crater, and finally involved Tarissan crater in 1997 with an increase since 1999 [6–8]. Since 1992, the volcano observatory has recorded a systematic and progressive increase in shallow low-energy seismicity, significant development of three acid-sulfate thermal springs at the SW base of the volcano with a slow rise of temperatures [9], and most noticeably, a significant increase in summit fumarolic activity associated with HCl-rich and H_2S acid gas emanations [6,7]. Currently there is no significant fumarolic activity at the base of the dome except weak non-pressurized emanations from the stable areas of Morne Mitan and Route de la Citerne.

Numerous geological works were carried on the volcano [2,6–8] and a good knowledge of its history is now obtained. During its construction, La Grande Découverte – La Soufrière volcano has experienced a series of flank-collapse events [2,3,6,10,11], particularly during its recent stage, making this volcano one of the most unstable of the world. The last one occurred probably at the beginning of the 1440 AD eruption and the lava dome is built inside a small horseshoe-shaped crater opened to the South as the precedent ones. Evidence from the geological record indicates that in the last 15,000 yrs the frequency of partial edifice collapse has increased although the volume of the collapses has decreased. Several factors suggest that the Soufrière lava dome is locally mechanically weak and thus pre-disposed to flank instability: 1) numerous fractures formed and reactivated during phreatic eruptions, 2) faults, 3) morphological constraints (steep slope), 4) the pervasive extensive hydrothermal alteration of parts of the Soufrière dome, 5) the reactivation of the hydrothermal system involving acid fluids, 6) a ring of thermal springs at the base of the lava dome with a discharge rate that can reach several kilogrammes per second. These springs promote the development of head-ward erosion in concave embayments.

Detailed geophysical imaging of the upper part of volcano edifices is of primary importance for the interpretation of data provided by the permanent sensors networks influenced by the heterogeneous character of the medium [12]. Self-potential measurements are among the most widely used geophysical observables to monitor the activity of volcanoes [13–17], and a correct interpretation of these data needs the knowledge of the electrical conductivity distribution [18,19].

Mechanical and dynamic modelling of the stability of the lava dome and its potential partial collapse requires a better knowledge of its past activity but also of its internal structure. Moreover, obtaining volumetric estimates of the mechanically weak areas susceptible to collapse within the lava dome as well as of the hydrothermal active cells susceptible to participate to a phreatic explosion remain key objectives for any improved hazard and risk analysis concerning the future evolution of the lava dome.

In this study, a geophysical imaging of the lava dome is made by electrical tomography. Direct current electrical profiles are achieved using a multielectrode data acquisition system connected to cables with 64 electrode plugs. 5 or 15 m electrode spacing provides a total layout of more than 300 or 900 m long, and the depth of investigation may reach a few hundred meters. Profiles made of several hundreds of measurements cross the lava dome, on the top, the flanks and around the base. The data are integrated in pseudo-sections of apparent

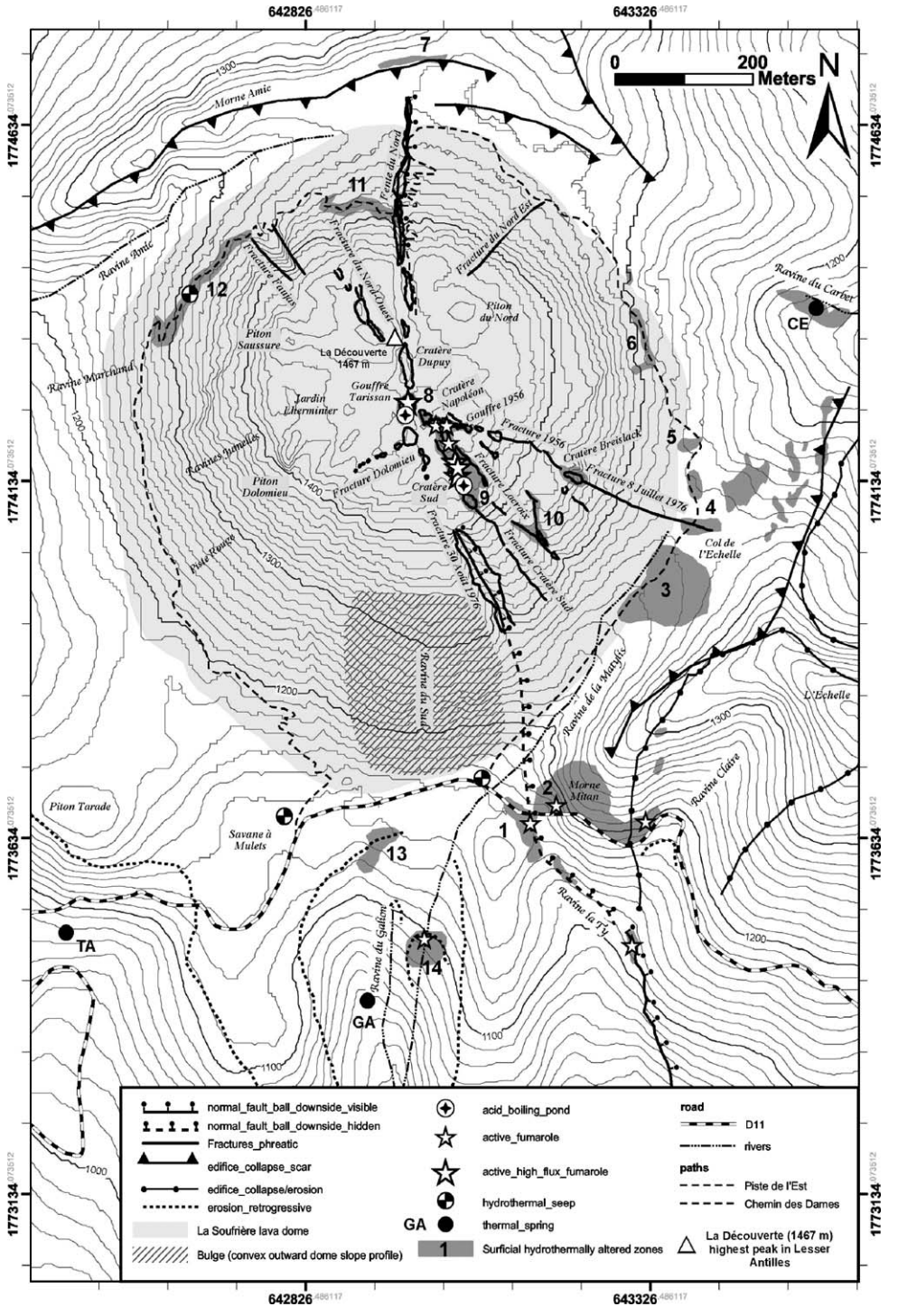

Fig. 1. Location map of the Soufrière lava dome with morphostructures, manifestations of the hydrothermal system and common sites (see insert legend). Hydrothermally altered and fumarolic areas: (1) Route de la Citerne, (2) Morne Mitan, (3) Forage-Col de l'Échelle, (4) Col de l'Échelle (Soufleur, Chaudières), (5) Fumerolles du Carbet I, (6) Fumerolles du Carbet II, (7) Fumerolles Collardeau, (8) Napoléon, (9) Cratère Sud and Lacroix–Napoléon fumerolles supérieur, (10) Fumerolles Lacroix inférieur, (11) Fente du Nord, (12) Faujas-Chemin des Dames, (13) Bains Chauds du Galion, (14) Fumerolle de la Matylis. Primary latitude and longitude graduations in 500 m (WGS84 geodetic system, UTM20N projection).

resistivity providing a preliminary electrical image of the lava dome. Present and fossil hydrothermal zones appear with very low values of resistivity, and generally, all the profiles show an decrease in apparent resistivity with depth. At the present stage of the study, a 3D inversion of the whole data set is not possible because of a lack of data in some areas and because of difficulties to implement numerical methods for processing a very large number of data in a large domain with strong resistivity contrasts. However, 1D inversions of data subsets belonging to laterally invariant regions provide a quantitative assessment of resistivity values and depths of interfaces between layers of different conductivities. These results are also used to check the consistency of both the apparent resistivities and apparent depths used to represent the data in pseudo-sections.

2. Field experiment

We have periodically undertaken electrical tomography experiments on La Soufrière de Guadeloupe volcano since the end of 2001. The data acquisition was done with a fast multi-electrode ABEM system (Terrameter SAS4000 and Electrode Selector ES464) driving cables equipped with 64 plugs to connect grounded stainless-steel electrodes. The multi-electrode system possesses a relay matrix switcher which allows to arbitrarily choose the two electrodes used to inject the electrical current in the ground and the two electrodes to measure the electrical potential. Hereafter, according to the traditionally acknowledged terminology, the current electrodes are denoted by the *A* and *B* letters while letters *M* and *N* are for the potential electrodes. Two sets of cables are used during the field operations, one with an electrode spacing of 5 m and another one with a spacing of 15 m, providing total lengths of 315 and 945 m, respectively. These lengths can further be increased by inserting additional plug-less cables with a total length of 340 m. These additional cables may also be used to install the data acquisition system at a more convenient place depending on the local field conditions (e.g. fumaroles or very rugged topography and steep

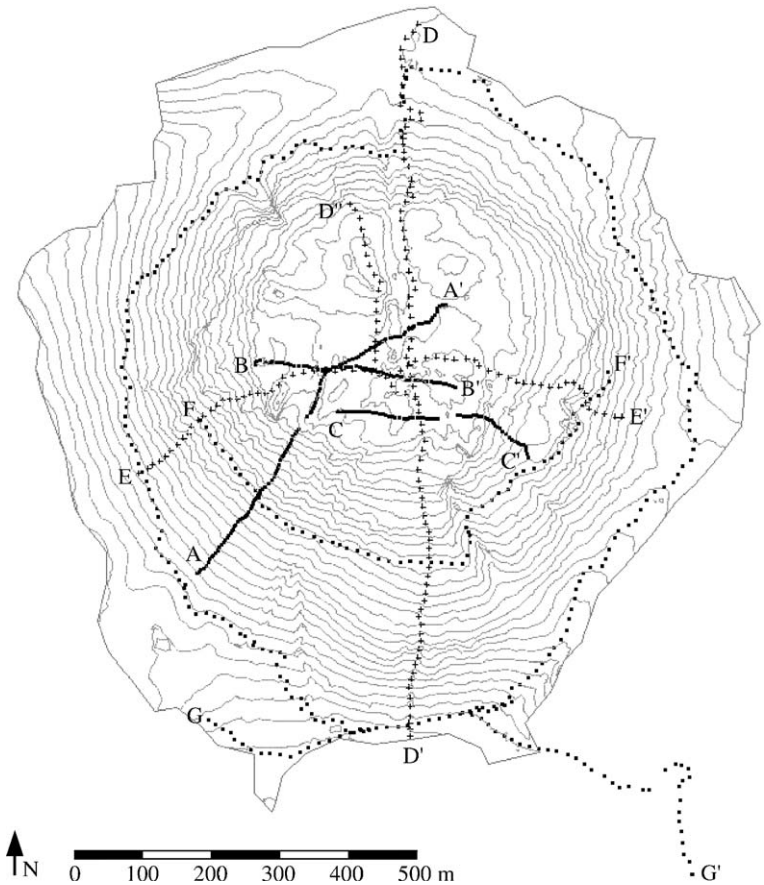

Fig. 2. Location of the electrical tomography profiles realised on the lava dome.

slopes). Also, one or two remote electrodes may be placed about 600 m away by using light single-channel cables. By this way, the electrical current may be injected on opposite sides of the volcano in order to sound its deeper parts.

Fig. 2 shows the location of the profiles achieved by the end of year 2004. These profiles are actually obtained by merging individual profiles done with either the 5-m or the 15-m cables. Each point on Fig. 2 represents a GPS electrode position. Profiles AA', BB' and CC' were obtained with the 5-m cables providing data with a high spatial resolution. The remaining profiles were done with the 15-m cables, providing greater depth of investigation. The location of the cables is strongly controlled by very difficult field conditions which sometimes necessitate rope access techniques. The final choice of a profile layout is guided by the accessibility conditions (paths and gullies, meteorological conditions). The northern side of the volcano remains poorly covered because of very rough topography and dense vegetation cover. The southern side of the lava dome is more accessible essentially because a large part of the vegetable cover has been suppressed by the acid gas cloud coming from the Cratère Sud fumarole. Profiles AA', DD' and EE' cover flanks of the lava dome, following a path on the northern part of profile DD', gullies on the southern part of profile DD' and on the western part of profiles AA' and EE'. These profiles cross the top of the lava dome over various azimuths. Also on the top of the lava dome, profile CC' crosses the Cratère Sud zone. The gap in the middle of this latter profile is due to the additional plug-less cables used to install the apparatus at a safe remote place.

For each cable layout, measurements are made for an ensemble of $\{A,B,M,N\}$ combinations chosen in order to perform an as-best-as-possible scanning of the subsurface both in the vertical and the horizontal directions. Among the many combinations achievable, we retained those minimising the number of $\{A,B\}$ pairs in order to have a number of numerical direct problems as small as possible to solve during geo-electrical modelling. Our general survey strategy is to perform a number of quasi 2D tomographic slices whose merging will ultimately constitute a data set to obtain a global 3D geo-electrical tomography of the lava dome. This 3D imaging of the lava dome should ideally be done through a global full 3D inversion, an enormous task which is not yet achieved at the present stage of our work. However, the data set presently obtained already allows to propose a first glance at the 3D geo-electrical structure of the lava dome in order to locate its principle compartments (basal layer, fractures and craters, hydrothermal zones, fluid circulation, etc.). This is done by performing a 3D arrangement of 2D pseudo-sections of the electrical resistivity. Although approximate, this approach may be assessed both by checking its self-coherency and by quantitatively comparing it to 1D geo-electrical soundings.

3. Pseudo-sections of electrical resistivity

As explained in the previous section, we choose to produce an approximate 3D image of geo-electrical structure of the lava dome by performing a 3D assemblage of quasi-2D pseudo-sections of the electrical resistivity. We agree that pseudo-sections do not reproduce the actual geometry of structures and may suffer from strong distortions. However, provided that the self-consistency of the pseudo-sections is verified, we believe that their 3D assemblage is useful to provide information about the 3D structure of the lava dome.

Pseudo-sections are widely used to display apparent-resistivity data by arranging them in a natural order where each measurement is placed at a point P located at a depth proportional to the size of the quadrupole of electrodes [20,21]. The simplest cases of electrode arrays are for electrodes aligned along a straight profile

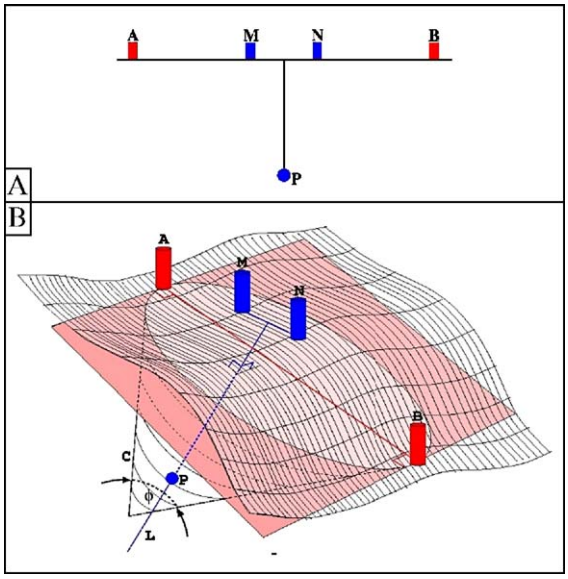

Fig. 3. (A) For conventional electrode arrangements (here a Schlumberger array), pseudo-sections of apparent resistivity are constructed by placing each data point at a point P located at the middle of the array and at a depth proportional to the distance AB. (B) Method for constructing 3D pseudo-sections of apparent resistivity: We define a cone C with an apex angle $\phi=120°$. Its planar circular basis contains the current electrodes A and B and is horizontal in the direction perpendicular to the line (A,B). Next, a line L perpendicular to the cone basis and passing through the middle of the segment $[M,N]$ (potential electrodes) is drawn. Finally, the apparent resistivity value is associated to the point $P=L\cap C$.

over a half-space. An example is given in Fig. 3A for the so-called Schlumberger array for which the point P is located at the middle of the quadrupole and at a depth proportional to the distance AB. A set of measurements corresponding to different positions and sizes of the quadrupole is used to construct a pseudo-section map by placing a pixel at each point P with a colour depending on the apparent resistivity. The apparent resistivity is derived from the measured resistance by multiplying it by a geometrical factor which depends on the distance between the electrodes forming the quadrupole. For an homogeneous medium, the so-obtained apparent resistivity equals the true resistivity.

The case of pseudo-sections for curved profiles and electrodes placed over a 3D irregular topography is less common, and we now explain how the pseudo-sections discussed hereafter are constructed. As for classical pseudo-sections corresponding to aligned electrodes (Fig. 3A), the main idea is that the larger the size of the quadrupole the greater the depth range corresponding to the measured apparent resistivity. In a first stage (Fig. 3), a cone C with an apex angle $\phi = 120°$ is defined. Its planar circular basis contains the current electrodes A and B and is horizontal in the direction perpendicular to the line (A,B). In a second stage, a line L perpendicular to the cone basis and passing through the middle of the segment $[M,N]$ (the potential electrodes) is drawn. Finally, the apparent resistivity value is associated to the point $P = L \cap C$. For too-curved profiles and strongly misaligned electrodes, the intersection between the cone C and the line L no more exists and no point P can be assigned to the corresponding measurement. The procedure then only works for arrangements with almost collinear electrodes and with the midpoint between the M and N electrodes located in between A and B. This condition implies that only a subset of the whole data set can be processed in this manner. The geometrical factors used to convert the electrical potential data to apparent

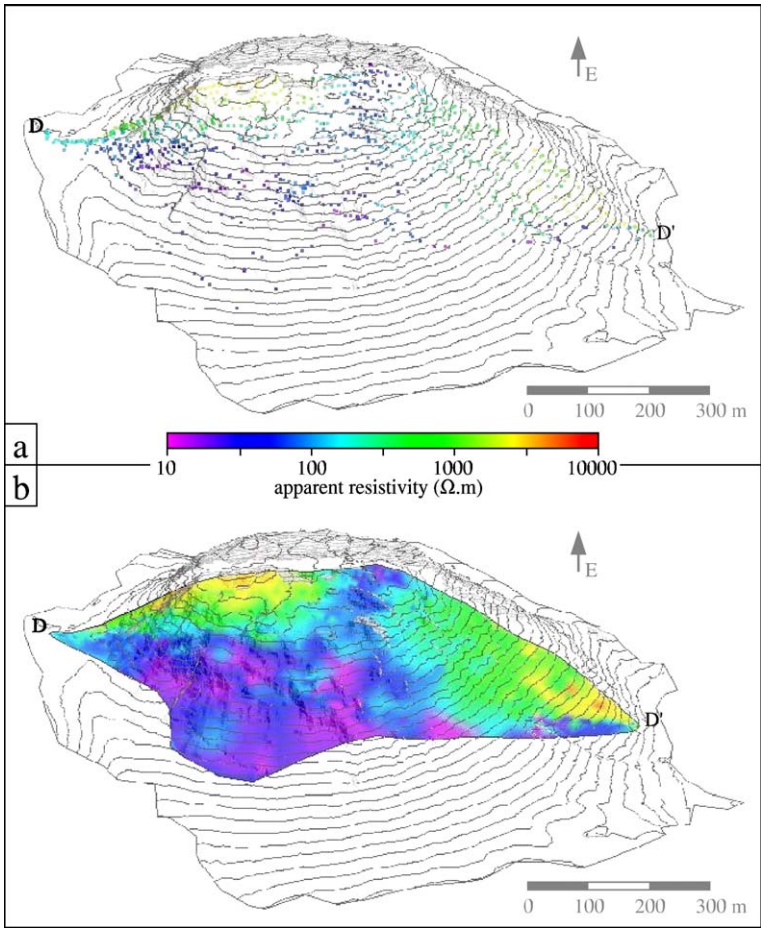

Fig. 4. Pseudo-section of apparent resistivity for profile D–D′ seen from the south-west side of the volcano: (a) the points of measurement set on the 3D domain; (b) interpolation on a warped surface.

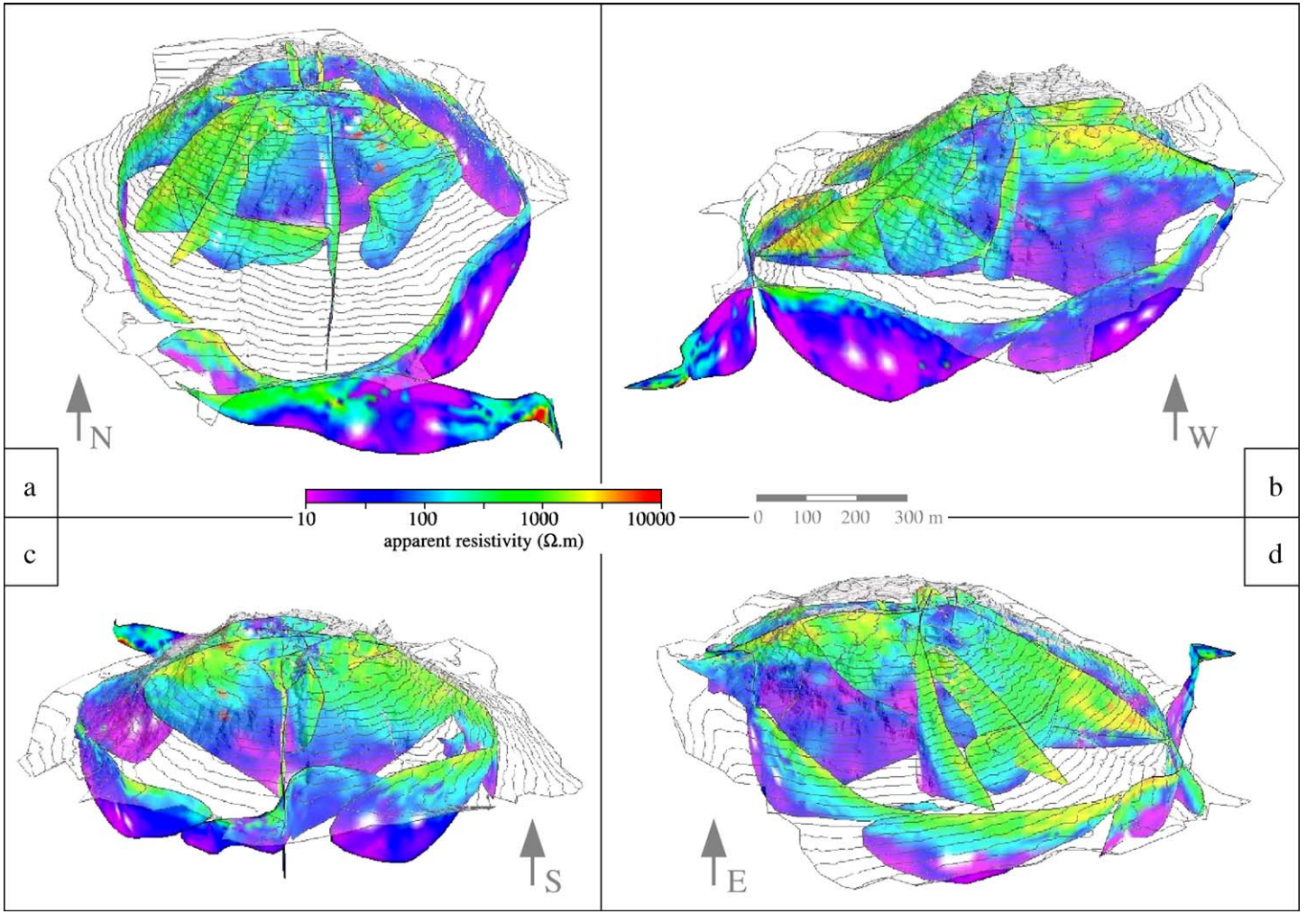

Fig. 5. Pseudo-sections of apparent resistivity for all the profiles, with a point of view of 30° elevation and (a) toward the North, (b) toward the West, (c) toward the South, (d) toward the East.

resistivities are computed by assuming a plane geometry and by using the actual distances between the electrodes.

Fig. 4 shows the pseudo-section of the apparent electrical resistivity corresponding to the DD' profile shown in Fig. 2. The set of points P associated with each acceptable $\{A,B,M,N\}$ electrode arrangement is shown in Fig. 4a. As explained above, each point received a colour in relation to the measured apparent resistivity. These points may be used to produce an interpolated pseudo-section as shown in Fig. 4b. It must be kept in mind that interpolation may eventually fill regions with a sparse distribution of points. We account for this limitation in the interpretation given in a next section.

By performing various 2D synthetic modellings with a topography identical to the one of the lava dome, we checked that the so-produced pseudo-sections are not affected by either strong distortions or important resistivity bias. We observed that the most important variations produced by the geometrical effects on the apparent resistivity values do not exceed a factor of 2. Although this might appear important at the first sight, this error factor is negligible when compared to the variations of apparent resistivity obtained with the real data and which span several orders of magnitude. Furthermore, the geometrical patterns of the distortions produced by topographic effects are totally different from what is observed in the real pseudo-sections. The results of the modelling are further validated by the comparison with the 1D geoelectrical soundings discussed in the next section.

The full 3D assemblage of the pseudo-sections for the profiles of Fig. 2 is shown in Fig. 5 for different azimuths. A common logarithmic colour scale spanning 3 orders of magnitude for the resistivity is used for easier comparison. It can be observed that the individual pseudo-sections are mutually very coherent in regions where they intersect each other. This agreement constitutes an a posteriori validation of the geometrical representation used to construct the pseudo-sections.

4. 1D inversions

4.1. Parameterization of the inverse problem

Several parts of the pseudo-sections shown in Fig. 5 display a 1D-like structure where the resistivity varies only in the z direction. In such cases, we invert the data under the 1D approximation to obtain vertical resistivity soundings in order to locally check for the quality of the pseudo-sections. In particular, it is possible to verify that the thicknesses of resistive layers and the values of apparent resistivity in the pseudo-sections are reasonable with respect to the inverted resistivity soundings.

Numerous studies have been devoted to 1D geoelectrical inversions where the unknown parameters to be determined are the thicknesses, Δz_n, and conductivities, σ_n, of the $n=1,\cdots,N$ layers forming the resistivity structure overlying a half-space with conductivity σ_0 [22–24]. However, in the present study we want to not only perform a 1D inversion to obtain the Δz's and the σ's, but we also want to test the validity of the 1D approximation. Consequently, we formulate the inverse problem to be solved as follows: find the best 1D resistivity model $\mathbf{m}$ with the largest data subset $\mathbf{d}_{1D}$ compatible with the 1D approximation. The subset $\mathbf{d}_{1D}$ counts K elements extracted from a larger data set $\mathbf{d}$ corresponding to a region where the pseudo-section has a 1D appearance. In what follows, we present a non-linear inversion method where $\mathbf{m}$ and $\mathbf{d}_{1D}$ are simultaneously inverted.

The model vector is defined as

$$\mathbf{m} = \{\ln\sigma_0,\ln\sigma_1,\cdots,\ln\sigma_N,\Delta z_1,\cdots,\Delta z_N\}, \quad (1)$$

with the logarithms of the conductivities taken as the unknown parameters. This parameterization is often recommended because of the large range spanned by the conductivity values. Also, the logarithmic parameterization gives an equivalent role to both the conductivity and the resistivity which are reciprocal physical quantities [25]. The logarithm of the conductivity is a fundamental quantity which appears in the integral equation formulation of the Poisson equation giving the perturbations of the electrical potential caused by conductivity heterogeneities [26].

The data vector, $\mathbf{d}$, consists in the logarithms of the resistance measurements $R_I=\Delta V_I/I_I$ where ΔV_I is the electrical potential measured between electrodes M and N, and I_I is the electrical current injected between electrodes A and B. Because of the large range spanned by the electrical potential measurements, some renormalization is necessary and, in the present study, we apply a weighting by dividing each data by the logarithm of the squared geometrical factor deduced from the electrode arrangement. By this way, all data have almost the same magnitude and weight equivalently in the misfit estimate.

In practice, the model selection relies on the maximisation of the following likelihood function,

$$L(\mathbf{m},\mathbf{d}_{1D}) \propto \left(\exp\left[-\frac{|\mathbf{d}_{1D}-\mathbf{d}_{\mathbf{m}}|_1}{S}\right]\right)^{K^{-\alpha}}, \quad (2)$$

where $|\cdot|_1$ stands for the L_1 norm, $\mathbf{d}_{\mathbf{m}}$ is the synthetic data vector produced by the 1D conductivity model $\mathbf{m}$, K is the dimension of the data subset actually used to evaluate the fit with the model, and $\alpha=3$ is an exponent

experimentally chosen to apply a penalty to models fitted with a relatively small number of data. By this way, Eq. (2) allows to compare models fitted with a variable number K of data taken in the initial data set. The standard deviation, S, is initially chosen equal to unity.

4.2. Inversion by simulated annealing

The search for the best model, $\mathbf{m}_{\text{best}}$, and its corresponding data subset, $\mathbf{d}_{1D,\text{best}}$, is performed with the simulated annealing algorithm which easily allows to

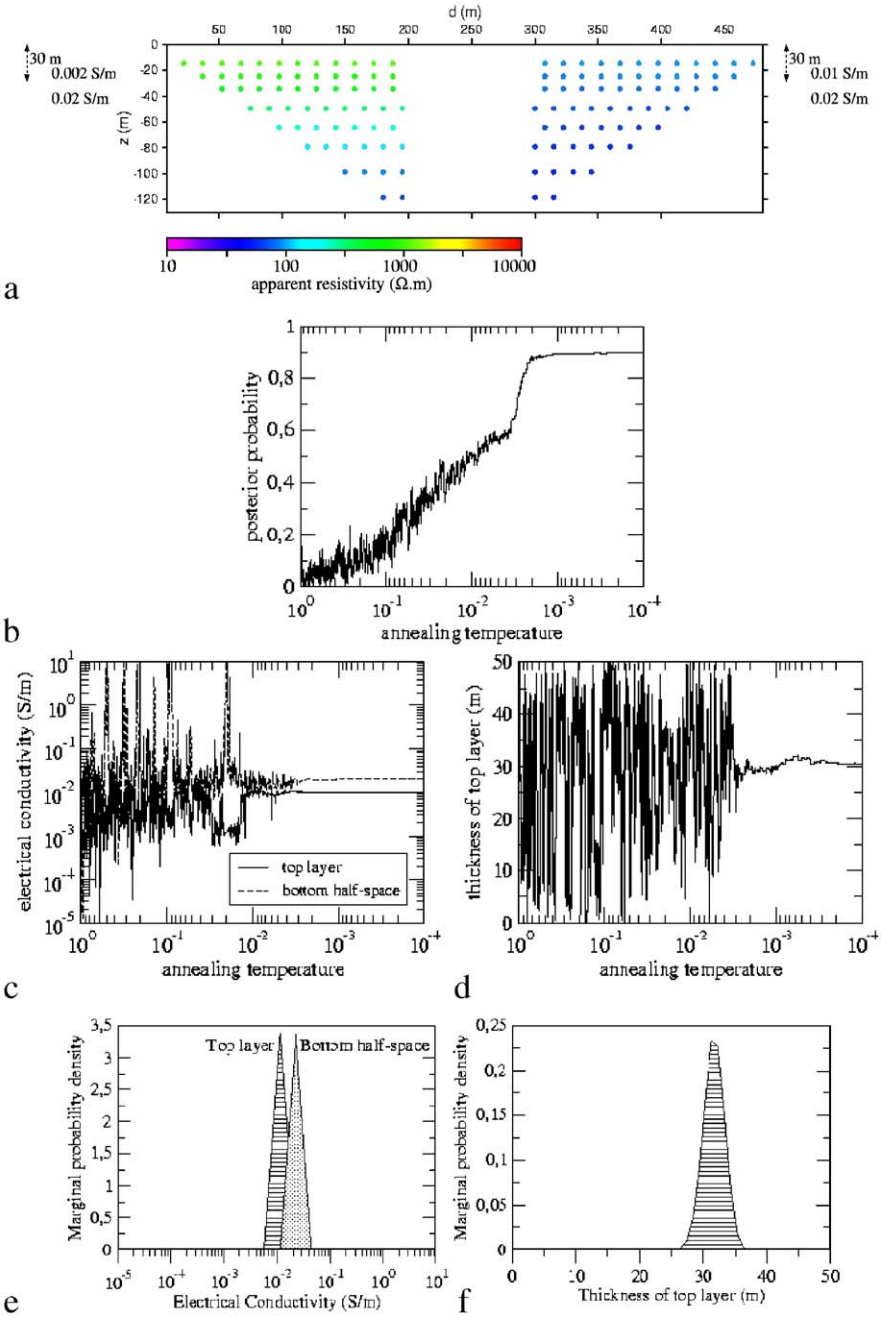

Fig. 6. 1D inversion process of synthetic data: (a) the inverted pseudo-section is obtained by merging two data subsets corresponding to two models of conductivity shown on the left and on the right parts of the figure; (b) likelihood curve of the models forming the Metropolis chain versus annealing temperature; (c) electrical conductivity versus annealing temperature; (d) top layer thickness versus annealing temperature; (e) probability distribution of the conductivities of the final model; (f) probability distribution of the top layer thickness of the final model.

tackle with sophisticated likelihood functions as in Eq. (2). In the following, we shall only give the technical details specifically adjusted for the present study, and the reader is referred to [26–30] for general considerations concerning the Metropolis and the simulated annealing algorithms in the framework of non-linear inversion.

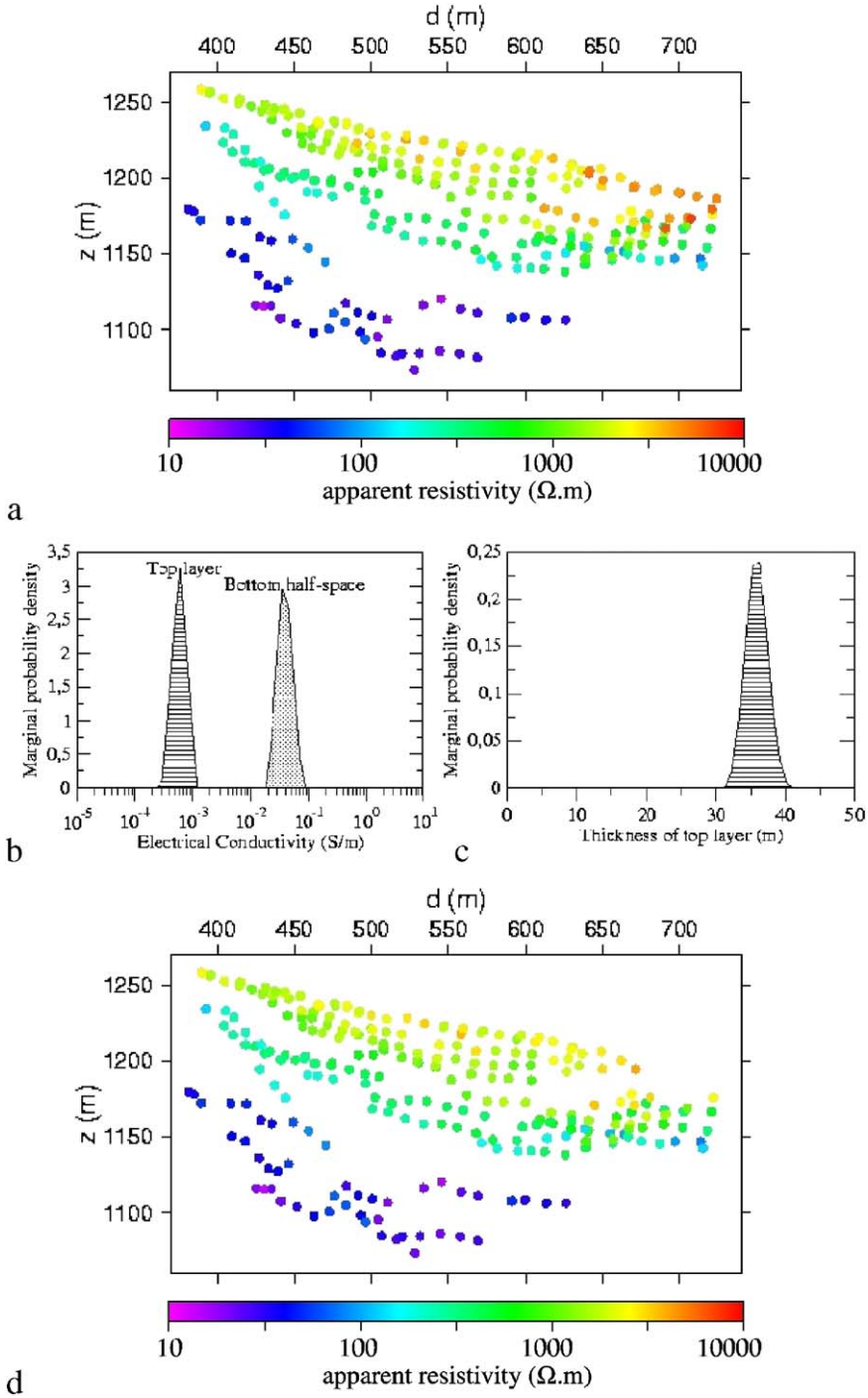

Fig. 7. 1D inversion results of the western part of the profile achieved around the base of the lava dome, along Chemin des Dames: (a) pre-selected data set; (b) probability distribution of the conductivities of the final model; (c) probability distribution of the top layer thickness of the final model; (d) data set consistent with the final model.

Let us recall that simulated annealing consists in doing Metropolis loops while applying a topological transformation to L by varying a control parameter traditionally called the temperature $T>0$ [26,31,32]. The transformed likelihood reads,

$$L_T(\mathbf{m},\mathbf{d}_{1D}) = L^{1/T}(\mathbf{m},\mathbf{d}_{1D}). \quad (3)$$

The simulated annealing loops begin with $T\to\infty$ for which L_∞ equals a constant and finish at $T=1$, i.e. at the likelihood given by Eq. (2). For each temperature T, a Metropolis loop is performed to generate a sequence of models distributed according to L_T. In practice, this consists in generating a sequence of models where the next model, $(\mathbf{m}, \mathbf{d}_{1D})_{j+1}$, to be added in the sequence is obtained from the preceding one, $(\mathbf{m}, \mathbf{d}_{1D})_j$, according to the random choice,

$$\text{prob}[(\mathbf{m},\mathbf{d}_{1D})_{j+1} = (\mathbf{m},\mathbf{d}_{1D})_{\text{try}}] = \min\left[1, \frac{L_T(\mathbf{m},\mathbf{d}_{1D})_{\text{try}}}{L_T(\mathbf{m},\mathbf{d}_{1D})_j}\right], \quad (4)$$

where $(\mathbf{m}, \mathbf{d}_{1D})_{\text{try}}$ is a candidate model which may eventually be included in the sequence of models. Eq.

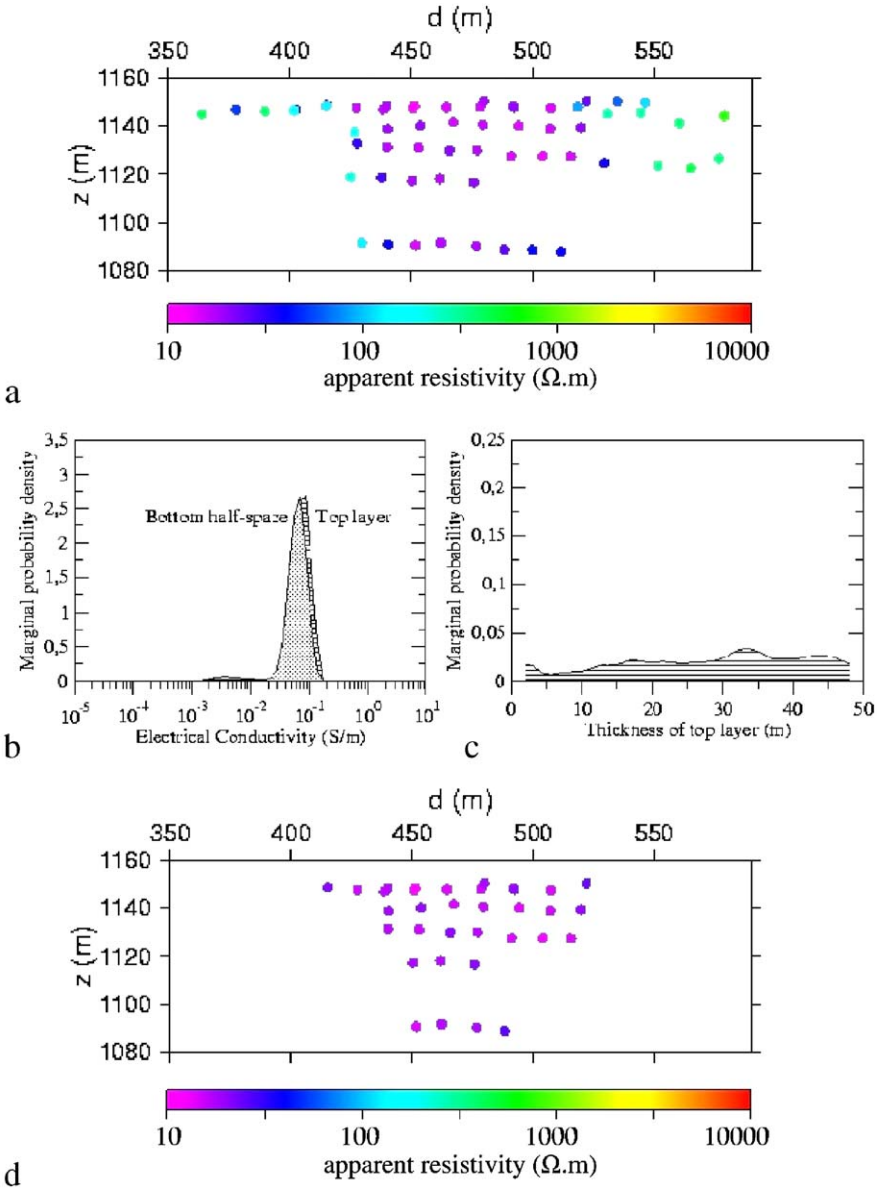

Fig. 8. 1D inversion results of a part of the profile G–G′ selected in the fumarolic area: (a) pre-selected data set; (b) probability distribution of the conductivities of the final model; (c) probability distribution of the top layer thickness of the final model; (d) data set consistent with the final model.

(4) indicates that a more-likely model is always accepted and that a less-likely model is sometimes accepted. When the random assignment given by Eq. (4) fails, i.e. when the less-likely candidate model has been rejected, the replicating transition $(\mathbf{m},\ \mathbf{d}_{1D})_{j+1}=(\mathbf{m},\ \mathbf{d}_{1D})_j$ is used instead. As the Metropolis loop proceeds, a sequence of models is generated such that more models fall in the most likely regions of the space model. As the temperature is lowered, these regions have their likelihood dramatically (i.e. exponentially) augmented, and if the temperature decrease is sufficiently slow, the chain of models is gently guided toward the regions of the space models where the likelihood is maximum [27,29].

The candidate model, $(\mathbf{m},\ \mathbf{d}_{1D})_{try}$, is obtained by perturbing the current model $(\mathbf{m},\ \mathbf{d}_{1D})_j$ in order to give some memory to the Metropolis chain. This point is of a particular importance in order not to make the algorithm a simple Monte Carlo search. The data subset $\mathbf{d}_{1D,try}$ of the candidate model is obtained by the following way: first we assign $\mathbf{d}_{1D,try}=\mathbf{d}_{1D,j}$ and next, in 50% of the time, a data element is randomly chosen in the whole data set d and is deleted from $\mathbf{d}_{1D,try}$ if present and is incorporated if absent. Hence, the data subset of the candidate model differs of at most one element with respect to the data subset of the last model in the Metropolis chain. The remaining parameters of the candidate model, namely the log-conductivities and the layer thicknesses, are obtained by randomly choosing a parameter, either log-conductivity or thickness, and by randomly perturbing it in a limited range.

4.3. Examples

We now discuss a synthetic example showing how the algorithm performs in presence of an incoherent data set whose elements were generated with two different conductivity structures. For this purpose, we invert the data set obtained by merging two synthetic data subsets of apparent resistivities computed for two different conductivity distributions (Fig. 6a). In a first stage the inversion is done with no estimate of the standard deviation S which is then set to unity. The annealing schedule is performed with a temperature range $1>T>10^{-4}$ in order to converge toward the most likely model. Fig. 6b shows the likelihood of the models successively incorporated in the Metropolis chain. The resulting curve is typical of the convergence property of simulated annealing: the chain starts with randomly chosen models with a low likelihood and with strongly varying parameter values as shown in Fig. 6c and d. As the temperature further decreases, the retained models progressively get a higher likelihood until the curve reaches a sharp step. At this stage of the cooling schedule, the model sequence suddenly gets confined in a region of high-likelihood models and the parameter values cease to strongly fluctuate (Fig. 6c and d). The success of the global convergence of simulated annealing toward the global maximum of L is controlled by the speed of cooling which must be sufficiently low to allow an exhaustive search in the space model. Once the best model is obtained, the residuals are used to compute an estimate of S, and the last step of the simulated annealing algorithm consists in a heat–bath sequence (i.e. a Metropolis chain constructed at a constant temperature) performed at $T=1$. The distribution of the models forming the heat–bath sequence may be used to construct the marginal probability curves [31,33,34] for each parameter as shown in Fig. 6e and f. Depending on the random assignments made in the Metropolis algorithm, the model sequence converges toward either of the two models used to construct the synthetic data set.

Fig. 7 shows the result of an inversion performed with a data subset extracted from the pseudo-section located on the western side of the volcano (Fig. 2). The marginal probability curves (Fig. 7b and c) indicate a two-layer conductivity structure with a resistive layer, $\rho_1\approx 3000\ \Omega$ m and $\Delta h_1\approx 35$ m, overlying a half-space with a resistivity $\rho_0\approx 50\ \Omega$ m. As can be observed in Fig. 7d, several data have been excluded from the original data set on the right side of the pseudo-section. Indeed, these data correspond to anomalous high apparent resistivity values incompatible with the assumed 1D geometry. Another example is shown in Fig. 8 for data

Table 1
Results from 1D inversions

Symbol	Name	ρ_1 (Ω m)	ρ_0 (Ω m)	Δz_1 (m)
A	Fumaroles	17	18	Unresolved
B	August 30th fracture	4400	40	10
C	Breislack	440	35	14
D	Col de l'échelle	910	60	10
E	Carbet	3400	70	8
F	Fente du Nord	1300	80	10
G	Faujas Landslide	3200	110	15
H	Chemin des Dames	2000	30	35
I	Tarade	1550	30	27
J	Ravine du Sud	1800	90	56
K	Gouffre 56	11200	230	7
L	Cratère Sud	360	250	Unresolved
M	Jardin Lherminier	100	500	3
N	Ravines Jumelles	2500	210	36
O	Piste rouge	2050	300	32
P	601	2150	230	31
R	Découverte	3350	Unresolved	28

corresponding to a fumarolic area. In this instance, the simulated annealing inversion gives marginal probabilities such that a simple half-space model is obtained with a resistivity $\rho_0 \approx 20\ \Omega$ m. Interestingly, the marginal probability curve for Δh_1 is flat, indicating that this parameter remains unresolved. The inverted data subset shown in Fig. 8d shows that lateral data corresponding to higher apparent resistivities have been automatically eliminated.

4.4. Results

A total of 17 data sets corresponding to almost 1D structures recognised in the pseudo-sections of Fig. 5 have been inverted according to the methodology described above. Several tests have been performed for models with more or less layers overlying the lower half-space to eventually represent a transition layer with variable resistivity. We found that models with two or more layers do not significantly improve the fit to the data. Moreover, increasing the number of layers often leads to models with low resistivity contrast and unresolved thicknesses. Consequently, according to the principle of parsimony, we decided to retain the simplest models, i.e. those with either one or no overlying layer, able to fit the data.

The results of the inversions are given in Table 1 and geographically displayed in Fig. 9. All but 3 data sets give a two-layer structure with a single layer overlying a

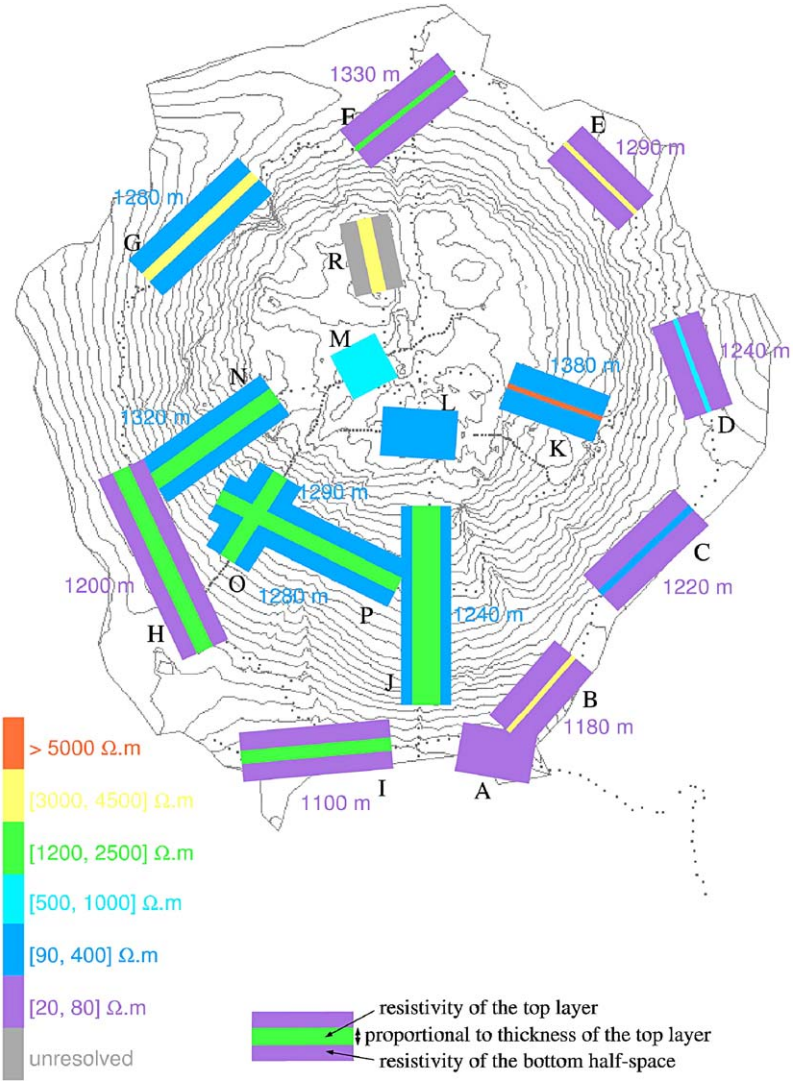

Fig. 9. Synthesis of the 1D inversion results obtained for 17 data subsets belonging to regions where the pseudo-sections appear laterally invariant. The great rectangle represents the resistivity of the bottom half space, the line represents the resistivity of the top layer and its thickness is proportional to the top layer thickness. The values of altitude correspond to the depth of the top of the conductive half space.

Table 2
List of areas where hydrothermally altered materials and old fumarolic fields are present and visible at the surface of the lava dome

Fumarolic area	Geographic site	Position	Age of activity	Type of activity
Cratère sud	Cratère sud fracture and crater	SE summit plateau	Most active highest flux	Pre-, syn-, post-eruptive
Tarissan	Tarissan crater	Central summit plateau	Active high flux	Pre-, syn-, post-eruptive
Napoléon	Napoléon crater	E summit plateau	Active moderate–low flux	Pre-, syn-, post-eruptive
Fumerolles Lacroix–Napoléon	Lacroix–Napoléon fracture	SE summit plateau	Active ? diffuse–low flux	Pre-, syn-, post-eruptive
Col de l'échelle	SE lava dome	Base of lava dome	Ceased 1984	Pre-, syn-, post-eruptive
Carbet fumerolles I and II	E–NE lava dome	Lower flanks of lava dome	Ceased 1979	Pre-, syn-, post-eruptive
Fumerolles Lacroix	E–SE lava dome	Upper flanks of lava dome	Ceased 1984	Pre-, syn-, post-eruptive
Forage échelle	E lava dome	Base of lava dome	Ceased 1984 ?	Pre-, syn-, post-eruptive
Fente du Nord	N lava dome	Upper flanks of lava dome	Ceased 1977 ?	Pre-, syn-, post-eruptive
Éboulement Faujas	NW lava dome	Upper flanks of lava dome	1797–98, 1837	Pre-, syn-, post-eruptive
Fumerolles Morne Mitan Matylis	SE lava dome	Periphery	Active low flux	Non-eruptive
Fumerolles ravine de la Ty	SE lava dome	Periphery	Active low flux	Non-eruptive
Fumerolles Collardeau	N lava dome	Outside (Amic dome)	Ceased 1982	Non-eruptive

In bold: Areas where the inverted 1D-conductivity structure corresponds to a high-conductivity (see Fig. 9).

more conductive half-space. The remaining two data sets correspond to an homogeneous half-space with no variations of conductivity in the vertical direction. They correspond on the lava dome to the Jardin Lherminier area, a shallow depression with a permanent small pond formed within relatively thick phreatic ash deposits, and to active fumarolic areas characterised by a high degree of hydrothermal alteration and up-flow of hydrothermal fluids located on the summit of the lava dome (Cratère Sud fumaroles) and at the South base of the lava dome near the road (Route de la Citerne fumaroles).

Fig. 9 reveals that the 17 geo-electrical soundings constitute a simple global conductivity structure with a low-resistivity ($\rho_0 \approx 50\ \Omega$ m) basal layer on the eastern and southern edges of the lava dome, and a medium-resistivity ($\rho_0 \approx 250\ \Omega$ m) basal layer on the northern edge and on the lava dome itself. In most cases, the basal layer is overlained by a resistive ($\rho_1 \approx 2000\ \Omega$ m) layer with a thickness Δh_1 comprised between 10 and 30 m. Noticeable exceptions are for the August 30th Fracture (B in Table 1) and the Carbet (E in Table 1) areas where the overlying layer has a significantly higher resistivity ($\rho_1 \approx 4000\ \Omega$ m) and corresponds to rock avalanche blocks. Another exception is for the Col de l'échelle (D in Table 1) area where the overlying layer has a lower resistivity ($\rho_1 \approx 400\ \Omega$ m) and corresponds to fumarolic zones that ceased to be active in 1979 and 1984 (see Table 2) [3,6,8].

5. Discussion

The geo-electrical structures revealed by both the pseudo-sections (Fig. 5) and the 1D inversions (Fig. 9) are very coherent and show strong resistivity contrasts depending on the particular geographical location on the volcano. Indeed, from one place to another, the resistivity varies over 3 orders of magnitude, and 3 main resistivity ranges may be identified: the low-resistivity range with $\rho \approx 20\ \Omega$ m, the medium-resistivity range with $\rho \approx 400\ \Omega$ m, and the high-resistivity range with $\rho \approx 2500\ \Omega$ m. Low resistivities are associated with either presently or historically active fumarolic zones where primary volcanic deposits have been strongly altered by the hydrothermal activity. A noticeable exception is for the Cratère Sud area which is the most active fumarole and where the resistivity is somewhat higher. This could be explained by the fact that hydrothermal activity has not yet lasted sufficiently to produce significant argilization or that the pH (acidity) and/or oxydo-reduction potential is not optimal for significant clay mineral production.

Basal layers with a medium resistivity correspond to several regions in the northern upper part of the lava dome where massive unaltered andesite is not covered by any significant altered lava or phreatic ash deposits. On the western flank of the lava dome, a medium resistivity layer is also found at depth below a layer of lower resistivity. This could be interpreted in terms of the presence at depth of more massive unaltered areas of the lava dome overlaid by a layer of thick better-drained scoriaceous or altered material (e.g. lava dome carapace, brecciated units formed during the formation of different lava flow lobes, variably vesicular zones related to lava extrusion processes) as seen in field outcrops and/or variably thick hydrothermally altered phreatic ashes from the historical eruptions.

The altitude of the conductive basal layer present on the eastern and southern sides of the lava dome varies

from 1290 m on the North to 1100 m on the South. This corresponds to an average southward slope exceeding 20%. A less-constrained similar slope is obtained for the south-west quarter of the lava dome from the west side (H in Table 1) geo-electrical sounding. Although a full 3D inversion has to be done before drawing definite conclusions, it can be observed that the deeper parts of the pseudo-sections (Fig. 5) indicate that the conductive basal layer seems to exist under a large part of the lava dome. This conductive basal layer can be interpreted in terms of volcanic structures. Its top likely corresponds to the floor of the horseshoe-shaped structure formed at the beginning of the 1440 AD eruption that resulted from a small flank-collapse event that destroyed the summit part of the volcano. Based on the abundance of hydrothermal products found in the resulting debris–avalanche deposits [11], this flank-collapse was probably favoured by an important hydrothermal alteration of the summit part of the volcano which can explain the presence of a thick conductive layer. Inside the horseshoe-shaped crater, the Soufrière lava dome was built. It is mainly constituted of massive lava of high resistivity signature.

The lava dome is cut by a series of fractures generated during the successive phreatic eruptions. These fractures favour the circulation of acid hydrothermal and meteoric fluids which progressively weather the massive lava and explain a signature of high conductivity of the fracture areas. It is probable that the alteration progresses as a function of the time. This can explain that the Cratère Sud, formed during the last phreatic eruption (1976–77), has a less conductive signature because of a lower state of hydrothermal alteration in spite of its current high fumarolic activity. Also, the conductive basal layer appears connected to a vertical conductive channel whose top part emerges in the Cratère Sud and the Tarissan areas. This might represent the pathway for the hydrothermal circuitry presently causing the very high fumarolic activity at the Cratère Sud and the more recent and yet moderate activity at Tarissan Crater [6–8].

6. Conclusion

The electrical tomography data discussed in the present paper reveal that La Soufrière of Guadeloupe lava dome consists of several 3D domains with relatively high resistivity separated by conductive channels. This electrical structure of the dome is coherent with the geological observations which indicate that the dome is made of unaltered massive andesite lava separated by major radial fractures that reach at least up to about half of the dome's height. The centre of convergence of these radial fractures corresponds to the Tarissan pit where increasing hydrothermal activity is observed, and which marks the northern limit of the presently active area of the dome. This active region, which concerns the south-eastern part of the dome summit, corresponds to a conductive channel visible on the pseudo-sections of Fig. 5 and extending down to a conductive layer located at the basis of the dome. This basis conductive layer is visible along most of the pseudo sections around the basis of the dome. When apparent at the surface, the conductive layer corresponds to highly hydrothermalized and altered geological materials with probably reduced internal friction and increased pore pressure. The 1D inversions give quantitative estimates of the depth of the conductive layer which constitutes a basal southward-inclined layer which is likely to contribute to the instability of parts of the edifice.

Acknowledgments

This work is dedicated to the memory of our Friend and Colleague Alberto Tarchini who participated to most of our field experiments and always shared his generous enthusiasm. This study benefited from invaluable help from the whole staff of the Observatoire Volcanologique et Sismologique de Guadeloupe: Christian Anténor-Habazac, Sara Bazin, Véronique Daniel, Bertrand Figaro, Gilbert Hammouya, Christian Lambert, Didier Mallarino and Laurent Mercier. D.G. and F. N. would like to thank Gérard Werther for numerous discussions concerning historical records about La Soufrière. Jean-Louis Le Mouël, Albert Tarantola and an anonymous reviewer made helpful reviews of drafts of this paper. Financial support was provided through the CNRS/INSU Antilles Program and from IPGP. This is IPGP contribution 2120.

References

[1] P.M. Vincent, N. Vatin-Perignon, M. Semet, J.L. Cheminée, Le dôme de la Soufrière (Guadeloupe), son âge et son mode de mise en place, C. R. Acad. Sci. Paris II 288 (1979) 51–54.

[2] G. Boudon, J. Dagain, M. Semet, D. Westercamp, Notice explicative de la carte géologique à 1/20 000 du massif volcanique de La Soufrière (Département de la Guadeloupe, Petites Antilles), BRGM, Paris, 1988, 43 pp.

[3] G. Boudon, M. Semet, P.M. Vincent, The evolution of La Grande Découverte (La Soufrière) volcano, Guadeloupe (F.W.I.), Volc. Hazards, Springer-Verlag, Berlin-Heidelberg, 1989, pp. 86–109.

[4] A. Barat, Etude du rôle des eaux souterraines dans le mécanisme des éruptions phréatiques. Application à la Montagne Pelée de Martinique et à La Soufrière de Guadeloupe, Thèse de spécialité, Univ. Bordeaux 3, 1984, 232 pp.

[5] J. Zlotnicki, G. Boudon, J.L. Le Mouël, The volcanic activity of La Soufrière of Guadeloupe (Lesser Antilles): structural and tectonic implications, J. Volcanol. Geotherm. Res. 49 (1992) 91–104.
[6] J.-C. Komorowski, G. Boudon, M. Semet, F. Beauducel, C. Anténor-Habazac, S. Bazin, G. Hammouya. Guadeloupe. In: J.M. Lindsay, S. Ali, R.E.A. Robertson, J.B. Shepherd and L. John (Eds), Volcanic Atlas of the Lesser Antilles, University of the West Indies, Seismic Research Unit, Trinidad, and IAVCEI (2005) 65–102.
[7] Observatoire Volcanologique et Sismologique de la Guadeloupe (OVSG), IPGP, Bilan Mensuel de l'Activité Volcanique et de la Sismicité régionale de l'Observatoire Volcanologique de la Soufrière, http://volcano.ipgp.jussieu.fr/guadeloupe/Infos.htm (1999–2005).
[8] J.-C. Komorowski, G. Boudon, C. Antenor-Habazac, G. Hammouya, M. Semet, J. David, Beauducel, J.-L. Cheminée, M. Feuillard, L'activité éruptive et non-éruptive de la Soufrière de Guadeloupe: problèmes et implications de la phénoménologie et des signaux actuellement enregistrés, INSU Lesser Antilles Volcanic Hazard Workshop, Paris, 18–19 janvier 2001, 2001, pp. 18–21, abstract volume.
[9] B. Villemant, G. Hammouya, A. Michel, M. Semet, J.-C. Komorowski, G. Boudon, J.-L. Chiminée, The memory of volcanic waters: shallow magma degassing revealed by halogen monitoring in thermal springs of La Soufrière volcano (Guadeloupe, Lesser Antilles), Earth and Planet. Sci. Lett. 237 (2005) 710–728.
[10] G. Boudon, M. Semet, P.M. Vincent, Flank failure-directed blast eruption at Soufrière, Guadeloupe, French West Indies: A 3,000-yr-old Mt. St. Helens? Geology 12 (1984) 350–353.
[11] J.-C. Komorowski, G. Boudon, M. Semet, B. Villemant, G. Hammouya, Recurrent flank-collapses at Soufrière of Guadeloupe volcano: implications of acid hydrothermal fluids on edifice stability Mount Pelée 1902–2002; Explosive volcanism in subduction zones, IPGP–INSU–IAVCEI International Congress, Martinique, mai 12–16 2002, p. 69, abstract volume.
[12] T. Kagiyama, H. Utada, T. Yamamoto, Magma ascent beneath Unzen Volcano, SW Japan, deduced from the electrical resistivity structure, J. Volcanol. Geotherm. Res. 89 (1999) 35–42.
[13] V.N. Pham, D. Boyer, G. Boudon, S. Gruszow, J. Zlotnicki, Anomalies de polarisation spontanée sur la Soufrière de Guadeloupe. Relations avec la structure interne du volcan, C. R. Acad. Sci. Paris II 310 (1990) 815–821.
[14] T. Hashimoto, Y. Tanaka, A large self-potential anomaly on Unzen volcano, Shimabara peninsula, Kyusyu island, Japan, Geophys. Res. Lett. 22 (1995) 191–194.
[15] J. Zlotnicki, Y. Nishida, Review on morphological insights of self-potential anomalies on volcanoes, Surv. Geophys. 24 (2003) 291–338.
[16] J. Zlotnicki, Y. Sasai, P. Yvetot, Y. Nishida, M. Uyeshima, F. Fauquet, H. Utada, H. Takahashi, G. Donnadieu, Resistivity and self-potential changes associated with volcanic activity: the July 8, 2000 Miyake-jima eruption (Japan), Earth Planet. Sci. Lett. 205 (2003) 139–154.
[17] K. Aizawa, A large self-potential anomaly and its changes on the quiet Mt. Fuji, Japan, Geophys. Res. Lett. 31 (5) (2004) L05612, doi:10.1029/2004GL019462.
[18] D. Gibert, M. Pessel, Identification of sources of potential fields with the continuous wavelet transform: Application to self-potential profiles, Geophys. Res. Lett. 28 (2001) 1863–1866.
[19] K. Aizawa, R. Yoshimura, N. Oshiman, K. Yamazaki, T. Uto, Y. Ogawa, S.B. Tank, W. Kanda, S. Sakanaka, Y. Furukawa, T. Hashimoto, M. Uyeshima, T. Ogawa, I. Shiozaki, A.W. Hurst, Hydrothermal system beneath Mt. Fuji volcano inferred from magnetotellurics and electric self-potential, Earth and Planet. Sci. Lett. 235 (2005) 343–355.
[20] L.S. Edwards, A modified pseudo-section for resistivity and induced polarization, Geophysics 42 (1977) 1020–1036.
[21] R.D. Barker, Depth of investigation of collinear symmetrical four-electrode arrays, Geophysics 54 (1989) 1031–1037.
[22] A. Gyulai, T. Ormos, A new procedure for the interpretation of VES data: 1.5D simultaneous inversion method, J. Appl. Geophys. 41 (1999) 1–17.
[23] E.A. Muiuane, L.B. Pedersen, Automatic 1D interpretation of DC resistivity sounding data, J. Appl. Geophys. 42 (1999) 35–45.
[24] T. Dahlin, The development of DC resistivity imaging techniques, Comput. Geosci. 27 (2001) 1019–1029.
[25] A. Tarantola, Elements for Physics: Quantities, Qualities, and Intrinsic Theories, Springer, Berlin, 2006 263 pp.
[26] M. Pessel, D. Gibert, Multiscale electrical impedance tomography, J. Geophys. Res. 108B1 (2003) 2054, doi:10.1029/2001JB000233.
[27] N. Metropolis, A. Rosenbluth, N. Rosenbluth, A. Teller, E. Teller, Equation of the state calculations by fast computing machines, J. Chem. Phys. 21 (1953) 1087–1092.
[28] S. Kirkpatrick, C.D. Gelatt, M.P. Vecchi, Optimization by simulated annealing, Science 220 (1983) 671–680.
[29] G. Bhanot, The Metropolis algorithm, Rep. Prog. Phys. 51 (1988) 429–457.
[30] M. Sambridge, K. Mosegaard, Monte Carlo methods in geophysical inverse problems, Rev. Geophys. 40 (3) (2002) 1009, doi:10.1029/2000RG00089.
[31] D. Gibert, J. Virieux, Electromagnetic imaging and simulated annealing, J. Geophys. Res. 96 (1991) 8057–8067.
[32] K. Mosegaard, A. Tarantola, Monte-Carlo sampling of solutions of inverse problems, J. Geophys. Res. 100 (1995) 12431–12447.
[33] D. Gibert, B. Tournerie, J. Virieux, High-resolution electromagnetic imaging of the conductive Earth interior, Inverse Probl. 10 (1994) 341–351.
[34] K. Mosegaard, Resolution analysis of general inverse problems through inverse Monte Carlo sampling, Inverse Probl. 14 (1998) 405–426.